

Anomalous octahedral distortion and multiple phase transitions in the metal-ordered manganite YBaMn_2O_6

T. Nakajima,^a H. Kageyama,^{a,*} M. Ichihara,^a K. Ohoyama,^c H. Yoshizawa,^b and Y. Ueda^a

^a *Materials Design and Characterization Laboratory, Institute for Solid State Physics, University of Tokyo, 5-1-5 Kashiwanoha, Kashiwa, Chiba 277-8581, Japan*

^b *Neutron Science Laboratory, Institute for Solid State Physics, University of Tokyo, 106-1 Shirakata, Tokai, Ibaraki 319-1106, Japan*

^c *Institute for Materials Research, Tohoku University, 2-1-1 Katahira, Aoba-ku, Sendai 980-8577, Japan*

Received 9 June 2003; received in revised form 24 September 2003; accepted 6 October 2003

Abstract

By means of powder X-ray diffraction, powder neutron diffraction and transmission electron microscopy (TEM), we determined the crystal structures of a metal-ordered manganite YBaMn_2O_6 which undergoes successive phase transitions. A high-temperature metallic phase ($T_{c1} = 520 \text{ K} < T$) crystallizes in a triclinic $P1$ with the following unit cell: $Z = 2$, $a = 5.4948(15) \text{ \AA}$, $b = 5.4920(14) \text{ \AA}$, $c = 7.7174(4) \text{ \AA}$, $\alpha = 89.804(20)^\circ$, $\beta = 90.173(20)^\circ$, $\gamma = 91.160(4)^\circ$. The MnO_6 octahedral tilting is approximately written as $a^0b^-c^-$, leading to a significant structural anisotropy within the ab plane. The structure for $T_{c2} < T < T_{c1}$ is a monoclinic $P2$ ($Z = 2$, $a = 5.5181(4) \text{ \AA}$, $b = 5.5142(4) \text{ \AA}$, $c = 7.6443(3) \text{ \AA}$, $\beta = 90.267(4)^\circ$) with an $a^-b^-c^-$ tilting. The structural features suggest a $d_{x^2-y^2}$ orbital ordering (OO). Below $T_{c2} = 480 \text{ K}$, crystallographically inequivalent two octahedra show distinct volume difference, due to the $\text{Mn}^{3+}/\text{Mn}^{4+}$ charge ordering. The TEM study furthermore revealed a unique $d_{3x^2-r^2}/d_{3y^2-r^2}$ OO with a modified CE structure. It was found that the obtained crystal structures are strongly correlated to the unusual physical properties. In particular, the extremely high temperature at which charge degree of freedom freezes, T_{c2} , should be caused by the absence of the structural disorder and by heavily distorted MnO_6 octahedra.

© 2003 Elsevier Inc. All rights reserved.

Keywords: Metal-ordered perovskite; YBaMn_2O_6 ; Charge/orbital ordering; Octahedral tilting; CE structure; X-ray and neutron diffraction; Transmission electron microscopy

1. Introduction

Manganese perovskites with a formula $A_{1-x}^{3+}A_x^{2+}\text{MnO}_3$ ($0 < x < 1$), where A^{3+} and A^{2+} represent in general rare-earth ions and alkaline-earth ions, respectively, have been extensively investigated for the past 10 years [1]. The potential application to the industrial technology has apparently accelerated the research activity, and as a result deepened our comprehension of this system. Now it is widely accepted that the dopant concentration x and the band width w (or the tolerance factor f) are dominant two parameters which enable us to systematically tune the magnetic and transport properties including the colossal magnetore-

sistance, charge ordering (CO) and orbital ordering (OO) [1].

However, probably underestimated to date or even neglected in many cases, has been the effect of randomness or compositional inhomogeneity in the crystal structure, which inevitably exists when we deal with solid solutions except the end members, $x = 0$ and 1. This effect may destroy some hidden phase which otherwise may be present at given x and $w(f)$. One also encounters difficulties in estimating the physical quantities precisely. In fact, ferromagnetic ordering temperatures observed experimentally so far have been much lower than that predicted theoretically [2].

This unfavorable situation can be avoided by preparing the case of $x = 0.5$, i.e., $AA'\text{Mn}_2\text{O}_6$, where the AO and $A'O$ layers are piled up alternately along the c axis, as illustrated in Fig. 1. In 1999, Millange et al. [3] succeeded in synthesizing an A -site metal-ordered manganite $\text{LaBaMn}_2\text{O}_6$ through a topotactic route and

*Corresponding author. Present address: Department of Chemistry, Graduate School of Science, Kyoto University, Kyoto 606-8502, Japan. Fax: +81-75-753-4000.

E-mail address: kage@kuchem.kyoto-u.ac.jp (H. Kageyama).

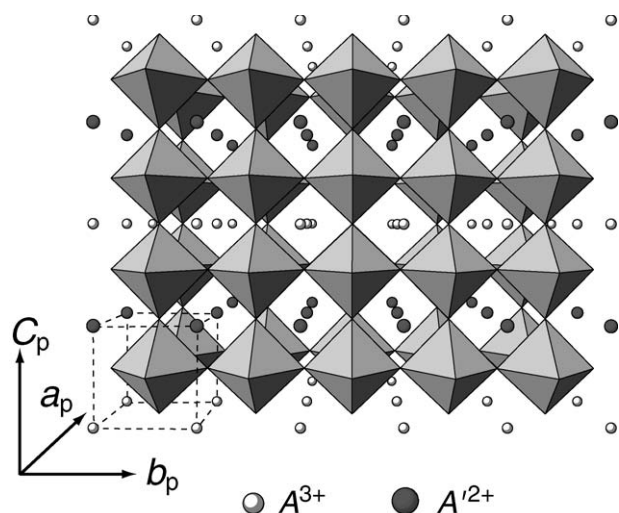


Fig. 1. Schematic representation of the ideal crystal structure of the A -site ordered manganese perovskite, $A^{3+}A'^{2+}Mn_2O_6$, showing the corner-shared MnO_6 octahedra. The open and solid balls are the A^{3+} and A'^{2+} ions, respectively. The broken lines denote the unit cell for the simple cubic perovskite with the A cation at the origin ($a_p \times b_p \times c_p$).

demonstrated that its ferromagnetic ordering temperature is 335 K which is indeed much higher than that for the metal-disordered correspondence ($La_{0.5}Ba_{0.5}MnO_3$) by 65 K.

Following this result, we prepared the next ‘clean’ manganite perovskite corresponding to $A=Y$, $A'=Ba$ and $x=0.5$ (i.e., $YBaMn_2O_6$) [4]. Rather preliminary structural analysis based on X-ray powder diffraction and physical properties obtained from magnetic susceptibility (χ) and electric resistivity (ρ) experiments suggest that $YBaMn_2O_6$ undergoes, unlike metal-disordered compound $A_{0.5}^{3+}A'_{0.5}{}^{2+}MnO_3$, multiple phase transitions as a function of temperature (T); upon cooling, a first-order-like structural transition occurs at $T_{c1} = 520$ K between paramagnetic and metallic phases ($PM_1 \rightarrow PM_2$). The second transition at $T_{c2} = 480$ K is a metal–insulator (MI) transition, and the last one at $T_{c3} = 200$ K induces the paramagnetic insulator (PI) to an antiferromagnetic insulator (AFI). Here, several prominent features merit to point out as follows: (a) The MI transition temperature T_{MI} ($=T_{c2}$) is, to the best of the authors knowledge, the highest among known manganese perovskite family. (b) In a striking contrast to the metal-disordered system [1], the structural transition at T_{c1} with drastic changes in lattice constants is not accompanied by the MI transition (i.e., $T_{c1} \neq T_{c2}$). (c) The structural transition at T_{c1} from a pseudo-orthorhombic to a pseudo-tetragonal symmetry on cooling is quite rare.

Moreover, a study of a series of the A -site ordered manganites $RBaMn_2O_6$ with R being Y and rare-earth elements has revealed that the phase diagram of $RBaMn_2O_6$ is considerably different from that of the

disordered analogue $A_{0.5}^{3+}A'_{0.5}{}^{2+}MnO_3$ [1,5]. It is thus evident that the structural and physical properties of $YBaMn_2O_6$ cannot be mapped onto such a simple framework that has been adequate for the disordered manganese perovskites [1]. The main purpose of the present study is the determination of the crystal structures of $YBaMn_2O_6$ in each phase on the basis of the Rietveld refinement using the powder neutron and X-ray diffraction data. As chemical characterizations, we performed the thermogravimetric analysis (TGA) and the differential scanning calorimetry (DSC). In order to observe possible superstructures due to the CO and OO, we used the transmission electron microscopy (TEM). The magnetic and transport properties were investigated by the magnetic susceptibility and electric resistivity measurements as a function of T . These intensive investigations have allowed us to unveil an intimate correlation between physical properties and underlying structures.

2. Experimental procedures

The synthesis of the A -site ordered perovskite $YBaMn_2O_6$ requires the following two procedures as employed for the homeotype of $LaBaMn_2O_6$ [4]. Starting reagents Y_2O_3 , MnO_2 , and $BaCO_3$ with 99.99% purities (Rare Metallic Inc.) were ground thoroughly, pressed into pellets and calcined in an Ar flow (6N) at 1573 K for 48 h. The use of Ar gas can avoid the formation of the A -site disorder. However, the obtained specimen contains a large amount of oxygen vacancy in the YO layer, providing $YBaMn_2O_{6-y}$ ($y \sim 0.9$) [6]. The metal ordering in the form of layers and the lack of oxygen in the YO layers are due to the general preference of the small Y^{3+} ions (and rare-earth ions) to take eight-fold coordination. The second step is annealing the obtained specimen in flowing O_2 at 773 K for 48 h, which leads to the full oxidation of the specimen, i.e., to $YBaMn_2O_6$. This reaction is reversible and indicates the topotactic nature of the transformation between $YBaMn_2O_5$ and $YBaMn_2O_6$.

The determination of the oxygen content of the final product was made by TGA using a TG2000S Mac Science analyzer. This experiment was performed in the T range between 300 and 1273 K with a heating rate 15–20 K/min in flowing H_2 . The DSC measurement was carried out on a DSC3200S Mac Science analyzer for $T = 140$ –600 K with the heating and cooling rate of 10–20 K/min. For the TGA (DSC) measurement, approximately 20 (30) mg of finely ground sample was placed in an aluminum (platinum) capsule, and well-calcined $\alpha-Al_2O_3$ was used as reference standard.

The X-ray powder diffraction experiments were performed using a MXP18 Mac Science diffractometer with the following operation conditions: $270 \text{ K} < T <$

600 K, $5^\circ < 2\theta < 120^\circ$ with the step size of 0.02° , $\text{CuK}\alpha$ radiation, $V = 50 \text{ kV}$ and $I = 300 \text{ mA}$. The neutron powder diffraction experiments were conducted for $200 \text{ K} < T < 600 \text{ K}$ using the Kinken powder diffractometer for high efficiency and high-resolution measurements, HERMES, at Institute for Materials Research (IMR), Tohoku University, installed at the JRR-3M reactor in Japan Atomic Energy Research Institute (JAERI), Tokai, Japan. Neutrons with a wavelength of 1.8196 \AA were obtained by the 331 reflection of the Ge monochromator. The $12'$ -blank-sample- $18'$ collimation was employed. The data were collected with a step-scan procedure in the range $2\theta = 10$ – 120° with a step width of 0.01° . The 1.5 g powder sample was wrapped by an Al foil to form a cylindrical shape ($8 \phi \times 15 \text{ mm}$) and then fixed to an Al sample holder with He gas filled.

The microscopic structures arising from the CO and OO in the PI phase were probed by means of TEM using JEM2010 (JEOL) operating at 200 kV at room temperature. The sample was finely ground under methanol then dispersed on Cu grids coated with holy carbon support films.

The magnetic properties were studied using a SQUID magnetometer between 5 and 700 K at a static magnetic field (H) of 0.1 T . The electric resistivity was measured using a well-sintered pellet for $T = 100$ – 620 K by a conventional four-probe technique.

3. Results

3.1. Powder X-ray diffraction

Shown in Fig. 2 is the X-ray powder diffraction pattern in the PI state, measured at 350 K . The obtained data contain a main product of YBaMn_2O_6 as well as a minor impurity of $\text{BaMnO}_{3-\delta}$ (less than 1.0%). With regard to YBaMn_2O_6 , we previously assigned the X-ray diffraction patterns for each phase to the monoclinic structure with the dimension of $a_p \times b_p \times 2c_p$ [4], where a_p , b_p and c_p denote the unit cell for the simple cubic perovskite. However, careful experiment and re-consideration of the observed peaks resulted in the monoclinic but a larger unit cell of $\sqrt{2}a_p \times \sqrt{2}b_p \times 2c_p$ as indexed in Fig. 2. It is to be noted that the 001 reflection at around $2\theta = 12^\circ$ indicates the doubling of the c parameter with respect to c_p and thus ensures the Y/Ba ordering in the form of layers. The result of the Rietveld refinement of the crystal structures for this and other phases will be provided in the proceeding subsections.

In a similar way, re-consideration of the X-ray diffraction pattern in the PM_2 phase led to the conclusion that the crystal structure has the monoclinic unit cell $\sqrt{2}a_p \times \sqrt{2}b_p \times 2c_p$, whereas the PM_1 phase was found to be the triclinic system with $\sqrt{2}a_p \times \sqrt{2}b_p \times 2c_p$.

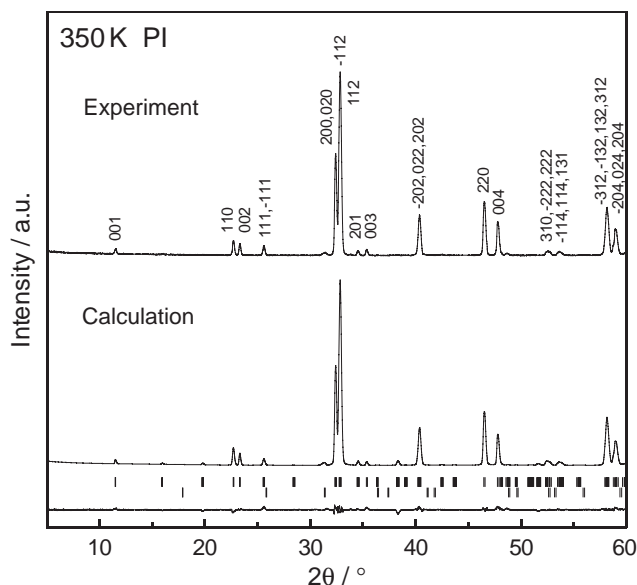


Fig. 2. (upper) The experimental powder X-ray diffraction pattern of YBaMn_2O_6 at 350 K (PI phase), indexed assuming the monoclinic unit cell with $\sqrt{2}a_p \times \sqrt{2}b_p \times 2c_p$. (lower) The calculated X-ray diffraction pattern. The upper and lower vertical marks show positions calculated for Bragg reflections for YBaMn_2O_6 and $\text{BaMnO}_{3-\delta}$, respectively. The lower trace is a plot of the difference between calculated and observed intensities.

We collected the powder X-ray diffraction patterns over a wide T range ($300 \text{ K} < T < 560 \text{ K}$), which covers the PI, PM_1 and PM_2 phases. After that, the lattice parameters were determined by the least-squares fitting, selecting well-isolated peaks at higher 2θ . The temperature variation of the reduced lattice constants (a_p , b_p , c_p), the angles (α , β , γ) and the unit-cell volume (V) is displayed in Fig. 3. The result is in general consistent with the previous result (Fig. 3 in Ref. [4]), although we assume the different crystal system for the PM_1 phase and the different unit-cell dimensions for all phases. It is easy to recognize discontinuous changes of the lattice parameters at T_{c1} , suggesting a first-order phase transition. In contrast, within our experimental accuracy the structural parameters, a_p , b_p , c_p , β (and V), are continuously changed at T_{c2} . However, it is noteworthy that the temperature dependence of V in the PI state is clearly different from that in the PM_2 state. These behaviors are consistent with the second-order-like transition at T_{c2} and are attributable to the change in electronic states by the MI transition.

3.2. Chemical characterizations and thermodynamic stability

From the TG experiment under H_2 flowing, the oxygen content of YBaMn_2O_6 was estimated to be the ideal stoichiometry 6.0 ± 0.02 per formula unit. Here, we measured the weight loss of the specimen after the

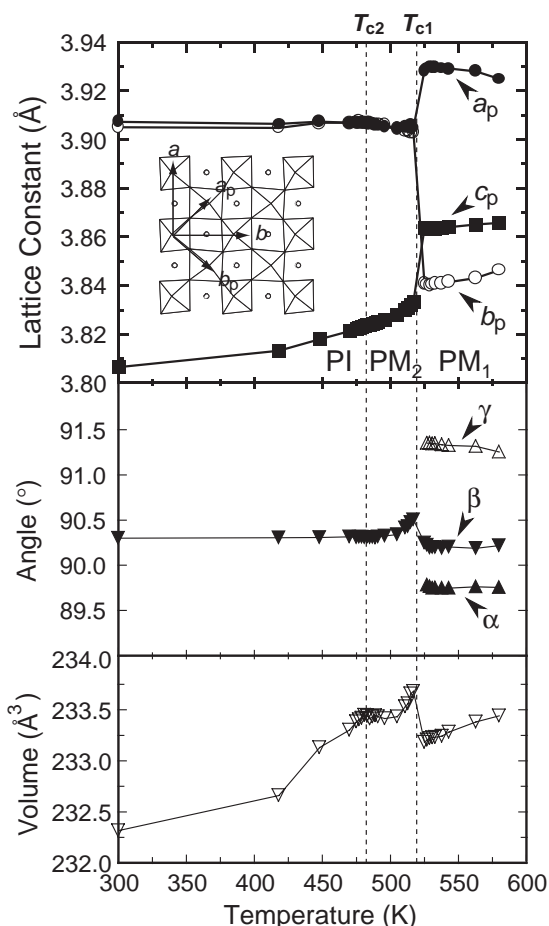


Fig. 3. Temperature dependence of the reduced lattice constants, (a_p , b_p , c_p), the angles (α , β , γ), and the volume (V), determined using a set of powder X-ray diffraction patterns, which were collected with increasing T . Estimated errors are within the size of each symbol.

following reaction: $\text{YBaMn}_2\text{O}_6 + 6\text{H}_2(\text{g}) \rightarrow (1/2)\text{Y}_2\text{O}_3 + \text{BaO} + 2\text{MnO} + (3/2)\text{H}_2\text{O}(\text{g})$. Complementary pieces of information were obtained by DTA and X-ray diffraction experiments, which clarified that annealing the specimen at relatively high temperatures in air destabilizes the metal-ordering in YBaMn_2O_6 . Namely, the anti-site disordering between the Y^{3+} and Ba^{2+} sites occurs at around 1100 K. The resultant phase, $\text{Y}_{0.5}\text{Ba}_{0.5}\text{MnO}_3$ with the A -sites being randomly distributed, irreversibly decomposes into YMnO_3 and BaMnO_3 at ~ 1300 K. When heated in turn under Ar gas flowing ($P_{\text{O}_2} < 1.5 \times 10^{-4}$ torr), the stoichiometric sample starts to release its oxygen at around 600 K, and finally reaches to $y \sim 0.5$ ($\text{YBaMn}_2\text{O}_{5.5}$) at 1000 K, as detected by the TGA experiment. Moreover, during the TEM experiments, where an extremely high vacuum ($P_{\text{O}_2} < 3 \times 10^{-8}$ torr) is achieved, we happened to find that the loss of oxygen in YBaMn_2O_6 starts at much lower temperature ~ 380 K. For this reason, it was unfortunately impossible to perform TEM to probe superstructures in the PM_1 and PM_2 phases.

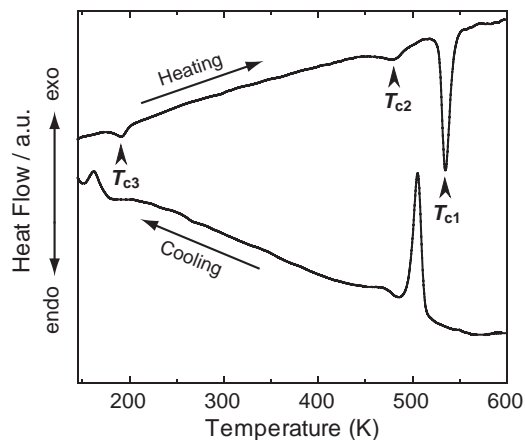


Fig. 4. Typical example of DSC curves of YBaMn_2O_6 taken with a heating/cooling rate of 20 K/min.

In Fig. 4, we represent a typical example of the DSC curve measured with the heating and cooling rate of 20 K/min. Upon heating, three endothermic reactions appear at 520, 480 and 195 K, nearly corresponding to the transition temperatures T_{c1} , T_{c2} and T_{c3} . Upon cooling, we observed respective three exothermic peaks. Reflecting the first-order phase transitions at T_{c1} and T_{c3} , the DSC peaks are observed at somewhat lower temperatures of 500 and 175 K than those in heating process, while the observed peak at 475 K is almost identical to that in heating process, indicating this transition to be nearly second order. These behaviors are in good accordance with the susceptibility and resistivity experiments to be mentioned later.

3.3. Magnetic and transport properties

We show the magnetic susceptibility and resistivity of YBaMn_2O_6 taken upon heating in Fig. 5 as solid curves. The χ exhibits a steep drop at T_{c1} , whereas a change in ρ at T_{c1} is subtle. In contrast, the ρ shows a drastic change at T_{c2} , while the χ is nearly unchanged across this temperature.

In the PM_1 and PI regimes, the χ behaves mostly in line with the Curie–Weiss law. The least square fitting to the Curie–Weiss formula in the PM_1 regime between 600 and 700 K gave the effective Bohr magneton $P_{\text{eff}} = 6.235(8) \mu_B$ and the Weiss temperature $\theta = 271.4(8)$ K (see the dotted line in Fig. 5). The obtained value of P_{eff} is close to the theoretical value $(P_{\text{eff}}^2(\text{Mn}^{3+}) + P_{\text{eff}}^2(\text{Mn}^{4+}))^{1/2} = 6.240 \mu_B$, where we assume the Mn^{3+} ($3d^4$) ions to take the high-spin configuration due to the stronger Hund coupling than the crystal field stabilization energy. The ferromagnetic spin–spin correlations derived from the positive θ supports the metallic conductivity associated with the so-called double exchange interaction.

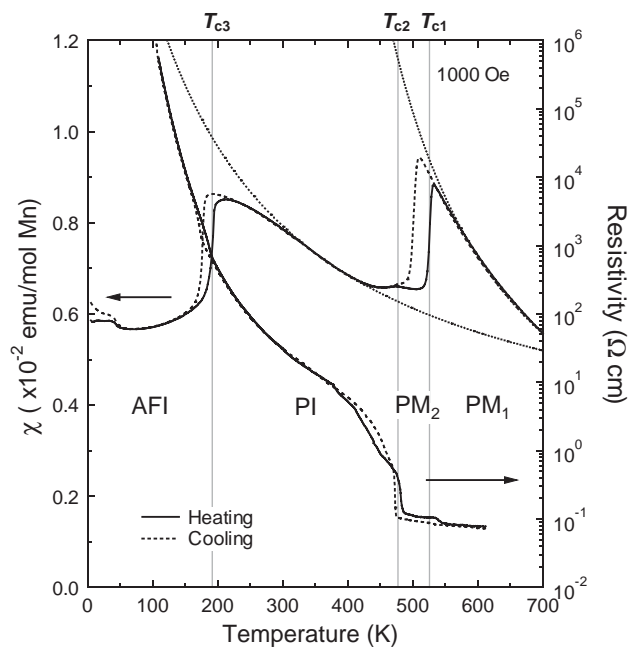


Fig. 5. Magnetic susceptibility and electrical resistivity of the polycrystalline sample of YBaMn_2O_6 as a function of T . Solid and broken curves represent, respectively, heating and cooling scans. The dotted lines represent the results of the Curie–Weiss fitting, performed in the PI and PM_1 regions (for details, see text).

In the PI state, we performed the Curie–Weiss fitting between 330 and 400 K, which gave a negative value of θ ($= -122.5(9)$ K), indicative of antiferromagnetic interactions. The antiferromagnetic spin–spin correlations below T_{c2} results in the Néel ordering at T_{c3} , at which a sudden reduction is observed in the χ – T curve. Our neutron diffraction experiment [7] indeed revealed Bragg reflections of magnetic origin, the intensities of which begin to glow at T_{c3} .

Broken curves in Fig. 5 represent the magnetic susceptibility and resistivity of YBaMn_2O_6 taken upon cooling. One finds distinct hystereses at T_{c1} and T_{c3} both in the χ – T and ρ – T curves, indicating these transition to be first order. Around T_{c2} , the cooling and heating processes coincide with each other within the experimental accuracy, suggesting the second-order-like transition. The χ shows a small upturn below 50 K, accompanied by small hysteresis. Since the neutron diffraction patterns do not show any change below and above this temperature, the magnetic structure must be almost identical and only a slight canting of the antiferromagnetically ordered moments may occur below T_{c3} .

3.4. Rietveld refinement

We show in Fig. 6(a) the neutron powder diffraction pattern measured at 350 K in the PI phase. All the peaks responsible for YBaMn_2O_6 can be successfully indexed,

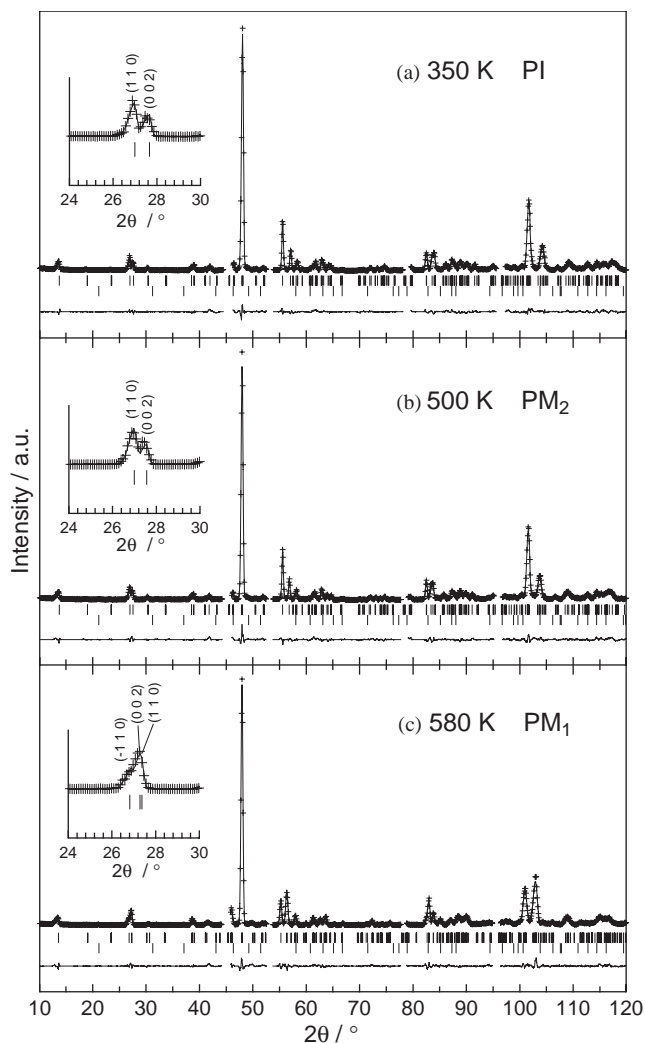


Fig. 6. Powder neutron diffraction profiles for YBaMn_2O_6 at: (a) 350 K, (b) 500 K and (c) 580 K. The calculated diffraction profiles are shown at the top with the solid line and the cross markers, respectively. The vertical marks in the middle show positions calculated for Bragg reflections. The lower trace is a plot of the difference between calculated and observed intensities. The second vertical marks for the impurity phase $\text{BaMnO}_{3-\delta}$. The signals from the Al foil wrapping the sample and/or the Al sample holder were excluded in the 2θ region. Insets: the enlarged plots for $24^\circ < 2\theta < 30^\circ$, to indicate that the use of the triclinic $P1$ space group is needed for (c).

using the monoclinic system with the same unit cell $\sqrt{2}a_p \times \sqrt{2}b_p \times 2c_p$ as that assumed in analyzing the powder X-ray diffraction pattern (Section 3.1). No extinction reflections both in the X-ray and neutron diffraction data allow us to arrive at a conclusion that only $P2$, Pm and $P2/m$ are possible among monoclinic space groups.

For oxides in general, the use of the neutron diffraction method has an advantage over the X-ray diffraction method in that the former can determine the positions of oxygen ions more precisely. This point should be particularly emphasized for the manganite perovskites, since oxygen bridging angles ($\angle \text{Mn-O-Mn}$)

between neighboring MnO_6 octahedra are known to play a crucial role in the physical properties [1]. The refinement of the crystal structure was therefore performed first by using the neutron diffraction data. The Rietveld method, implemented in the computer program RIETAN2000 developed by Izumi and Ikeda [8], was used. YBaMn_2O_6 was assumed to have the space group, either $P2$, Pm or $P2/m$, and $\text{BaMnO}_{3-\delta}$, detected as the impurity, was introduced in the calculations as the secondary phase. For each possible space group, we started the refinement with the initial atomic positions, referring to those of the metal-ordered but tetragonal system $\text{LaBaMn}_2\text{O}_6$ [3]. The R factors are defined as the following:

$$R_{\text{wp}} = \left[\frac{\sum_i w(|F_{i\text{o}}| - |F_{i\text{c}}|)^2}{\sum_i w|F_{i\text{o}}|^2} \right]^{1/2},$$

$$R_{\text{e}} = \left[\frac{(N - P)}{\sum_i w|F_{i\text{o}}|^2} \right]^{1/2},$$

$$R_{\text{I}} = \frac{\sum_K |I_{K\text{o}} - I_{K\text{c}}|}{\sum_K I_{K\text{o}}},$$

$$R_{\text{F}} = \frac{\sum_K |I_{K\text{o}}^{1/2} - I_{K\text{c}}^{1/2}|}{\sum_K I_{K\text{o}}^{1/2}},$$

where w is the weighing factor, $F_{i\text{o}}$ and $F_{i\text{c}}$ are the observed and calculated intensities, N is the total number of $F_{i\text{o}}$ data when the background is refined, P is the number of adjusted parameters, $I_{K\text{o}}$ and $I_{K\text{c}}$ are the observed and calculated integrated intensities.

In the course of the refinement, the isotropic temperature factors for each element were varied but constrained to be equal, in order to avoid correlation between the thermal and fractional occupancies. Setting oxygen occupancies as free parameters did not improve the result, so the oxygen ions are fixed to be fully occupied. This assumption is verified by the TG observation that the oxygen content is determined as 6.0 ± 0.02 . Consideration of fractional occupancies and anti-site disordering between the Ba^{2+} and Y^{3+} ions did not improve the result as well, which is understood in light of a significant difference in ionic radius between Y^{3+} and Ba^{2+} . The high quality and homogeneity of the specimen with the A -site ordering are supported by the distinct 7.5 \AA modulation along the $[001]_{\text{p}}$ spreading, without any notable fault, over a wide range of the $[100]_{\text{p}}$ -zone TEM image (Fig. 2(a) in Ref. [7]). All attempt to refine in Pm and $P2/m$ never results in the reliability factors better than 12%, and the obtained parameters such as bond lengths and angles were quite unrealistic. However, $P2$ quickly converged and gave reasonable structure as shown later on, providing by far the best reliability factors as follows: $R_{\text{wp}} = 9.87\%$, $R_{\text{e}} = 6.55\%$, $R_{\text{I}} = 4.96\%$ and $R_{\text{F}} = 2.90\%$. The observed, calculated and difference patterns from the

Rietveld refinement are displayed in Fig. 6(a) and the refined unit-cells parameters, positional coordinates, displacement parameters and refinement statistics are summarized in Table 1. Table 2 demonstrates selected bond distances and angles. The unit-cell parameters, $a = 5.5193(3) \text{ \AA}$, $b = 5.5131(3) \text{ \AA}$, $c = 7.6135(2) \text{ \AA}$ and $\beta = 90.295(3)^\circ$, agree well with those determined from the X-ray diffraction experiment. As a matter of fact, the X-ray diffraction pattern calculated using the parameters in Table 1 satisfactorily reproduce the experimental one (see Fig. 2).

There are crystallographically two inequivalent Mn sites, Mn(1) and Mn(2), and eight oxygen sites, O(1)~O(8). The oxygen arrangement around Mn(1) and Mn(2) is illustrated in Fig. 7(a). Two kinds of MnO_6 octahedron show a large distribution in $\angle \text{Mn-O-Mn}$ angles and a remarkable size difference as evidenced by the average Mn-O distances ($1.96(2) \text{ \AA}$ for Mn(1) and $1.93(2) \text{ \AA}$ for Mn(2)). This fact suggests that the Mn(1) and Mn(2) ions take, respectively, trivalent and tetravalent. Namely, the occurrence of the CO state like checkerboard in the ab plane is strongly anticipated at the MI transition temperature $T_{\text{c}2}$. This view is further supported by the bond valence sum calculation [9], which provides Mn(1) = +3.56, Mn(2) = +3.80, and will be confirmed by the TEM in Section 3.5.

The powder neutron diffraction data at 500 K (in the PM_2 phase) shown in Fig. 6(b) were successfully characterized, as in the case of the PI phase, by the monoclinic $\sqrt{2}a_{\text{p}} \times \sqrt{2}b_{\text{p}} \times 2c_{\text{p}}$ cell without any extinct reflections, and the Rietveld analysis gave the best fit ($R_{\text{wp}} = 10.15\%$, $R_{\text{e}} = 6.43\%$, $R_{\text{I}} = 5.07\%$ and $R_{\text{F}} = 3.06\%$) when one assumed $P2$ among $P2$, Pm and $P2/m$. The experimental and theoretical neutron diffraction patterns are compared in this figure, and the refined structural parameters are listed in Tables 1 and 2. The lattice parameters and the angle at 500 K solved are as follows: $a = 5.5181(4) \text{ \AA}$, $b = 5.5142(4) \text{ \AA}$, $c = 7.6443(3) \text{ \AA}$, $\beta = 90.267(4)^\circ$. The crystal structure of the PM_2 phase is similar to that of the PI phase in principle. However, the former phase differs from the latter in that the Mn(1) O_6 and Mn(2) O_6 octahedra have nearly the same size with the average Mn-O distances of $1.96(2)$ and $1.95(2) \text{ \AA}$, for Mn(1) and Mn(2), respectively, despite a rather large distribution in $\angle \text{Mn-O-Mn}$ angles in each octahedron. This observation is supported by the metallic conductivity above $T_{\text{c}2}$, where both Mn sites are supposed to take the valence of +3.5. It appears that the lack of change in symmetry at $T_{\text{c}2}$ is against crystallographic phase transition. However, as revealed by TEM (see Section 3.5), there is a translational symmetry breaking at $T_{\text{c}2}$ due to the formation of the CO/OO superstructure, enlarging the unit cell of the PI phase to $2\sqrt{2}a_{\text{p}} \times \sqrt{2}b_{\text{p}} \times 4c_{\text{p}}$. The shifts of atomic positions relevant to the structural modulations induced by the CO/OO of the CE type would be too small to be

Table 1

	Atom	Site	x	y	z	B_{iso} (\AA^2)
Temperature: 350 K	Y(1)	1c	0.5	0.041(5)	0	0.9(1)
Symmetry: monoclinic	Y(2)	1a	0	0.526(5)	0	0.9(1)
Space group: $P2$ (No. 3)	Ba(1)	1d	0.5	0	0.5	0.4(1)
$a = 5.5193(3)$ \AA	Ba(2)	1b	0	0.527(5)	0.5	0.4(1)
$b = 5.5131(3)$ \AA	Mn(1)	2e	0.018(3)	0.005(5)	0.242(2)	0.3(1)
$c = 7.6135(2)$ \AA	Mn(2)	2e	0.481(3)	0.518(6)	0.244(2)	0.3(1)
$\beta = 90.295(3)^\circ$	O(1)	1a	0	-0.017(5)	0	1.25(5)
$V = 231.67(2)$ \AA^3	O(2)	1c	0.5	0.575(6)	0	1.25(5)
$R_{\text{wp}} = 9.87\%$	O(3)	2e	0.279(2)	0.268(7)	0.195(1)	1.25(5)
$R_{\text{e}} = 6.55\%$	O(4)	2e	0.765(2)	0.271(7)	0.212(1)	1.25(5)
$R_{\text{I}} = 4.96\%$	O(5)	2e	0.247(2)	0.771(7)	0.237(2)	1.25(5)
$R_{\text{F}} = 2.90\%$	O(6)	2e	0.709(2)	0.798(6)	0.247(2)	1.25(5)
	O(7)	1b	0	0.051(6)	0.5	1.25(5)
	O(8)	1d	0.5	0.494(5)	0.5	1.25(5)
Temperature: 500 K	Y(1)	1c	0.5	0.000(7)	0	1.0(1)
Symmetry: monoclinic	Y(2)	1a	0	0.486(7)	0	1.0(1)
Space group: $P2$ (No. 3)	Ba(1)	1d	0.5	0	0.5	0.4(1)
$a = 5.5181(4)$ \AA	Ba(2)	1b	0	0.518(6)	0.5	0.4(1)
$b = 5.5142(4)$ \AA	Mn(1)	2e	0.026(4)	-0.005(8)	0.243(4)	0.3(1)
$c = 7.6443(3)$ \AA	Mn(2)	2e	0.492(5)	0.503(9)	0.242(4)	0.3(1)
$\beta = 90.267(4)^\circ$	O(1)	1a	0	-0.072(9)	0	1.32(6)
$V = 232.60(2)$ \AA^3	O(2)	1c	0.5	0.569(9)	0	1.32(6)
$R_{\text{wp}} = 10.15\%$	O(3)	2e	0.267(4)	0.249(8)	0.193(1)	1.32(6)
$R_{\text{e}} = 6.43\%$	O(4)	2e	0.766(3)	0.261(8)	0.215(1)	1.32(6)
$R_{\text{I}} = 5.07\%$	O(5)	2e	0.247(4)	0.752(8)	0.240(2)	1.32(6)
$R_{\text{F}} = 3.06\%$	O(6)	2e	0.715(3)	0.781(8)	0.244(2)	1.32(6)
	O(7)	1b	0	0.016(8)	0.5	1.32(6)
	O(8)	1d	0.5	0.468(8)	0.5	1.32(6)
Temperature: 580 K	Y(1)	1a	0.480(6)	-0.005(8)	-0.003(5)	1.1(1)
Symmetry: triclinic	Y(2)	1a	0.001(7)	0.488(7)	0.000(6)	1.1(1)
Space group: $P1$ (No. 1)	Ba(1)	1a	0.5	0	0.5	0.6(2)
$a = 5.4948(15)$ \AA	Ba(2)	1a	-0.014(6)	0.511(7)	0.502(5)	0.6(2)
$b = 5.4920(14)$ \AA	Mn(1)	1a	0.005(8)	0.001(8)	0.244(7)	0.4(2)
$c = 7.7174(4)$ \AA	Mn(2)	1a	0.488(9)	0.506(9)	0.235(6)	0.4(2)
$\alpha = 89.804(20)^\circ$	Mn(3)	1a	-0.002(9)	-0.005(8)	0.747(7)	0.4(2)
$\beta = 90.173(20)^\circ$	Mn(4)	1a	0.476(9)	0.496(9)	0.752(7)	0.4(2)
$\gamma = 91.160(4)^\circ$	O(1)	1a	0.041(8)	0.009(7)	0.011(5)	1.49(8)
$V = 232.83(8)$ \AA^3	O(2)	1a	0.432(8)	0.469(8)	0.000(6)	1.49(8)
$R_{\text{wp}} = 9.12\%$	O(3)	1a	0.214(7)	0.270(8)	0.269(6)	1.49(8)
$R_{\text{e}} = 6.22\%$	O(4)	1a	0.255(6)	0.774(7)	0.233(5)	1.49(8)
$R_{\text{I}} = 3.21\%$	O(5)	1a	0.718(7)	0.239(7)	0.226(6)	1.49(8)
$R_{\text{F}} = 1.78\%$	O(6)	1a	0.749(6)	0.739(8)	0.201(5)	1.49(8)
	O(7)	1a	-0.021(6)	-0.009(6)	0.495(5)	1.49(8)
	O(8)	1a	0.516(7)	0.533(7)	0.495(5)	1.49(8)
	O(9)	1a	0.254(7)	0.235(8)	0.756(5)	1.49(8)
	O(10)	1a	0.229(8)	0.743(8)	0.772(5)	1.49(8)
	O(11)	1a	0.751(7)	0.290(7)	0.802(6)	1.49(8)
	O(12)	1a	0.733(7)	0.780(8)	0.801(4)	1.49(8)

Positional parameters for YBaMn_2O_6 .

observed by powder X-ray and neutron diffraction experiments.

The Rietveld refinement for the neutron diffraction data at 580 K (in the PM_1 state) clarified that the structure has the triclinic $P1$ symmetry with the $\sqrt{2}a_p \times \sqrt{2}b_p \times 2c_p$ unit cell. The refinement statistics and unit-cell parameters are $R_{\text{wp}} = 9.12\%$, $R_{\text{e}} = 6.22\%$, $R_{\text{I}} = 3.21\%$, $R_{\text{F}} = 1.78\%$, $a = 5.4948(15)$ \AA , $b = 5.4920(14)$ \AA , $c = 7.7174(4)$ \AA , $\alpha = 89.804(20)^\circ$,

$\beta = 90.173(20)^\circ$, $\gamma = 91.160(4)^\circ$. The obtained parameters are summarized in Tables 1 and 2, and the experimental and calculated neutron diffraction patterns are shown in Fig. 6(c). The four inequivalent MnO_6 octahedra have the following average Mn–O distances: 1.93(8) \AA (Mn(1)), 1.94(8) \AA (Mn(2)), 1.96(8) \AA (Mn(3)), and 1.96(3) \AA (Mn(4)). Although the neutron diffraction patterns in Figs. 6(a)–(c) look similar to each other, a close look at the patterns, e.g., those around $2\theta = 27^\circ$

Table 2

Distances (Å)	$T = 350\text{ K}$		$T = 500\text{ K}$		$T = 580\text{ K}$	
					Distances (Å)	
Mn(1)–O(1)	$1.85(2) \times 1$	$1.90(2) \times 1$	Mn(1)–O(1)	$1.82(8) \times 1$	Mn(1)–O (average)	1.93(8)
Mn(1)–O(3)	$2.08(2) \times 1$	$1.97(3) \times 1$	Mn(1)–O(3)	$1.91(8) \times 1$	Mn(2)–O (average)	1.94(8)
Mn(1)–O(4)	$2.03(2) \times 1$	$2.06(3) \times 1$	Mn(1)–O(4)	$1.91(9) \times 1$	Mn(3)–O (average)	1.96(8)
Mn(1)–O(5)	$1.81(2) \times 1$	$1.81(3) \times 1$	Mn(1)–O(5)	$2.04(8) \times 1$	Mn(4)–O (average)	1.96(8)
Mn(1)–O(6)	$2.05(2) \times 1$	$2.07(2) \times 1$	Mn(1)–O(6)	$1.97(8) \times 1$		
Mn(1)–O(7)	$1.98(2) \times 1$	$1.96(3) \times 1$	Mn(1)–O(7)	$1.94(8) \times 1$	Angles (deg)	
Mn(2)–O(2)	$1.88(2) \times 1$	$1.89(3) \times 1$	Mn(2)–O(2)	$1.85(8) \times 1$	Mn(1)–O(1)–Mn(3)	164.6(9)
Mn(2)–O(3)	$1.80(2) \times 1$	$1.91(3) \times 1$	Mn(2)–O(3)	$1.98(9) \times 1$	Mn(2)–O(2)–Mn(4)	160.4(11)
Mn(2)–O(4)	$2.09(2) \times 1$	$2.03(3) \times 1$	Mn(2)–O(4)	$1.96(8) \times 1$	Mn(1)–O(3)–Mn(2)	162.0(10)
Mn(2)–O(5)	$1.90(3) \times 1$	$1.93(2) \times 1$	Mn(2)–O(5)	$1.95(8) \times 1$	Mn(1)–O(4)–Mn(2)	171.5(9)
Mn(2)–O(6)	$1.99(3) \times 1$	$1.97(3) \times 1$	Mn(2)–O(6)	$1.92(9) \times 1$	Mn(1)–O(5)–Mn(2)	170.1(9)
Mn(2)–O(8)	$1.95(2) \times 1$	$1.98(2) \times 1$	Mn(2)–O(8)	$2.02(8) \times 1$	Mn(1)–O(6)–Mn(2)	162.0(10)
Mn(1)–O (average)	1.96(2)	1.96(2)	Mn(3)–O(1)	$2.03(8) \times 1$	Mn(1)–O(7)–Mn(3)	173.9(9)
Mn(2)–O (average)	1.93(2)	1.95(2)	Mn(3)–O(7)	$1.94(9) \times 1$	Mn(2)–O(8)–Mn(4)	165.3(11)
			Mn(3)–O(9)	$1.90(8) \times 1$	Mn(3)–O(9)–Mn(4)	172.7(10)
Angles (deg)			Mn(3)–O(10)	$1.90(9) \times 1$	Mn(3)–O(10)–Mn(4)	169.6(9)
Mn(1)–O(1)–Mn(1)	172.4(7)	157.6(8)	Mn(3)–O(11)	$2.15(8) \times 1$	Mn(3)–O(11)–Mn(4)	153.6(11)
Mn(2)–O(2)–Mn(2)	161.8(8)	157.6(8)	Mn(3)–O(12)	$1.89(8) \times 1$	Mn(3)–O(12)–Mn(4)	155.4(10)
Mn(1)–O(3)–Mn(2)	157.5(8)	157.4(7)	Mn(4)–O(2)	$1.93(8) \times 1$		
Mn(1)–O(4)–Mn(2)	165.6(8)	167.2(7)	Mn(4)–O(8)	$2.00(8) \times 1$		
Mn(1)–O(5)–Mn(2)	176.8(8)	177.6(8)	Mn(4)–O(9)	$1.85(8) \times 1$		
Mn(1)–O(6)–Mn(2)	162.9(8)	163.2(7)	Mn(4)–O(10)	$1.94(9) \times 1$		
Mn(1)–O(7)–Mn(1)	165.1(7)	173.0(8)	Mn(4)–O(11)	$1.94(8) \times 1$		
Mn(2)–O(8)–Mn(2)	172.3(8)	169.0(8)	Mn(4)–O(12)	$2.12(8) \times 1$		

Selected bond distances and angles for YBaMn_2O_6 .

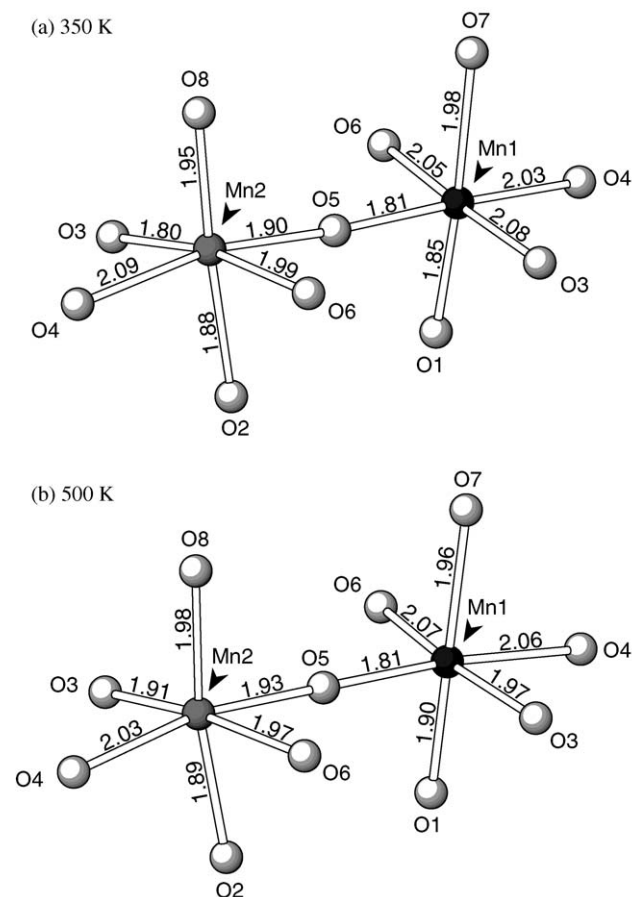


Fig. 7. The arrangement of oxygen ions around Mn at (a) 350 K and (b) 500 K, showing the Mn–O bond distances.

(compare the insets of Fig. 6) recognizes the necessity to employ the $P1$ space group for (c). In fact, the R factors never became better than 20, when the $P2$ symmetry was assumed.

Determination of the crystal structure below T_{c3} is difficult and still in progress partly because the transition involves the antiferromagnetic ordering with a four-fold periodicity along the c -axis (accompanied by the reformation of the CO/OO superstructure) [7]. Preliminary analysis indicates that the structure is also of monoclinic symmetry without any extinct reflections, giving $P2$, Pm and $P2/m$ as possible space groups.

3.5. Transmission electron microscope

In Figs. 8(a)–(d), we represent the $[001]_p$ -zone TEM image containing microtwinstructures and corresponding electron diffraction (ED) patterns, taken at room temperature (PI phase). The ED patterns taken from the areas A and C, include the satellite reflections with the commensurate structural modulations (q), written as $q_1 = (1/4, 1/4, 0)_p$ and $q_2 = (1/4, -1/4, 0)_p$, respectively. The ED patterns taken from the area B can be understood in terms of the superimposition of the two vectors. The formation of the twin structures is also visible in the image, which shows the contrasts of the corresponding superlattices. As one can see from Figs. 8(e)–(g), the ED patterns simulated by means of Digital Micrograph (Gatan) for the areas A, B and C nicely reproduce the experimental ED patterns.

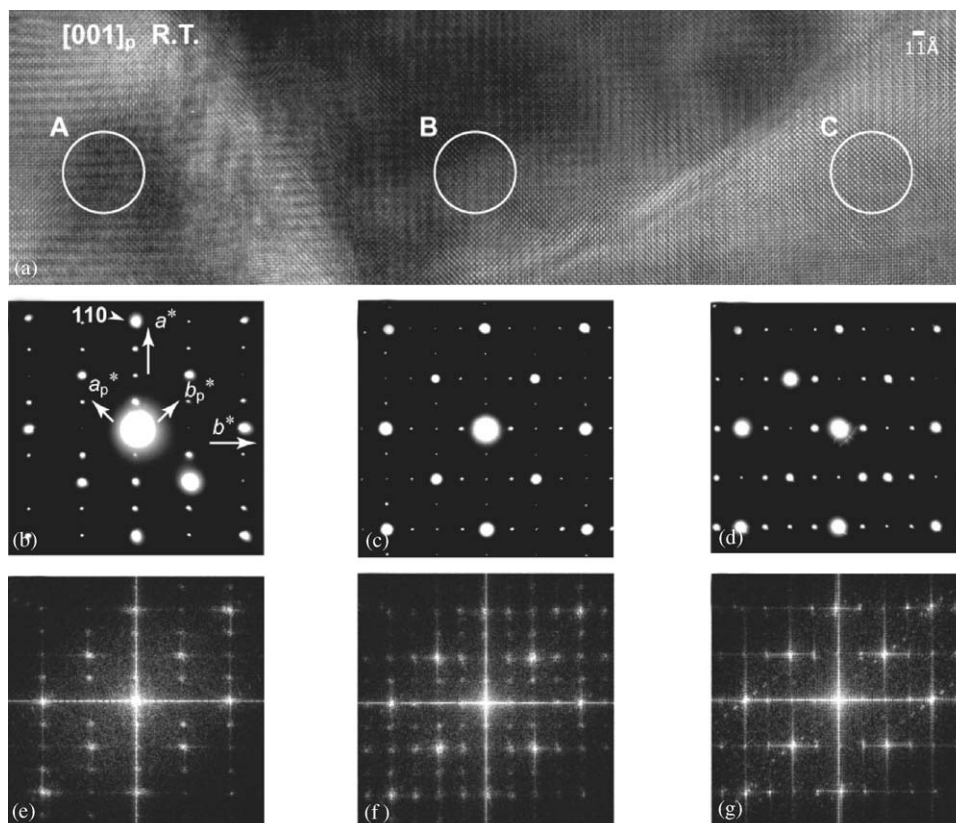


Fig. 8. (a) The $[001]_p$ zone TEM image at room temperature (PI phase), indicating the CE-type CO/OO ordering and the twin formation. (b)–(d) The observed ED patterns taken from the area A, B, and C. (e)–(g) The calculated ED patterns for the area A, B, and C.

Fig. 9(a) shows the $[100]_p$ -zone ED pattern, containing strong superlattice reflections with a two-fold periodicity along the c axis with respect to c_p . This originates from the Y/Ba ordering. In addition, we observed considerably weaker reflections with a four-fold periodicity along the same direction, enlarging the unit cell to $2\sqrt{2}a_p \times \sqrt{2}b_p \times 4c_p$. ED patterns are taken along various directions including $[011]_p$, $[021]_p$ and $[111]_p$ (see Figs. 9(b)–(d)), and the observed superreflections are plotted on the reciprocal lattice in Fig. 9(e). As we will demonstrate later, the observed superreflections are attributable to the CO and OO of a new kind.

4. Discussions

4.1. Heavily distorted MnO_6 octahedron

For conventional perovskites (ABO_3), wherein the A -sites are occupied by the single element and so are the B -sites, the BO_6 octahedra are almost always assumed to be rigid. Keeping its ideal shape, octahedra tilt so as to relax the size mismatch between the AO and BO_2 layers, typically when $f < 1$. More explicitly, sort and magnitude of the octahedral tilting depend not only on

the mismatch but also on coordination preference, covalency, etc. However, the obtained crystal structure of $YBaMn_2O_6$ cannot be described by such a simplified picture, as a result of an ultimate ionic size difference between Y^{3+} and Ba^{2+} ions. Considering the tolerance factors, $f_1 = 1.07$ for $\{A=Ba^{2+}$ and $B=Mn^{+3.5}\}$ and $f_2 = 0.92$ for $\{A=Y^{3+}$ and $B=Mn^{+3.5}\}$ [10], each MnO_2 layer in $YBaMn_2O_6$ should feel strain forces with the opposite signs (or a structural frustration) from the adjacent YO and BaO layers. Having this frustration, one can not achieve an adequate compensation for this structural mismatch solely from the tilting of the rigid MnO_6 octahedra. As a consequence, the shape of the MnO_6 octahedron deviates heavily from the ideal octahedron.

Fig. 10 demonstrates the $[110]_p$ projection of the crystal structure at 350 K. Reflecting the Y^{3+}/Ba^{2+} ordering in the form of layers, the averaged Y–O distance (2.592(9) Å) becomes shorter than the averaged Ba–O distance (2.875(9) Å). In other words, the MnO_2 planar oxygen ions (i.e., O(3), O(4), O(5), O(6)) are displaced largely from the ideal position $z = 0.25$ toward the YO layer. For a given octahedron, the averaged distances between oxygen ions of MnO_2 and YO layers are shortened ($\langle d_{O(pl)-O(ap)} \rangle = 2.62(3)$ Å for Mn(1) and 2.59(3) Å for Mn(2)), while those of MnO_2 and BaO

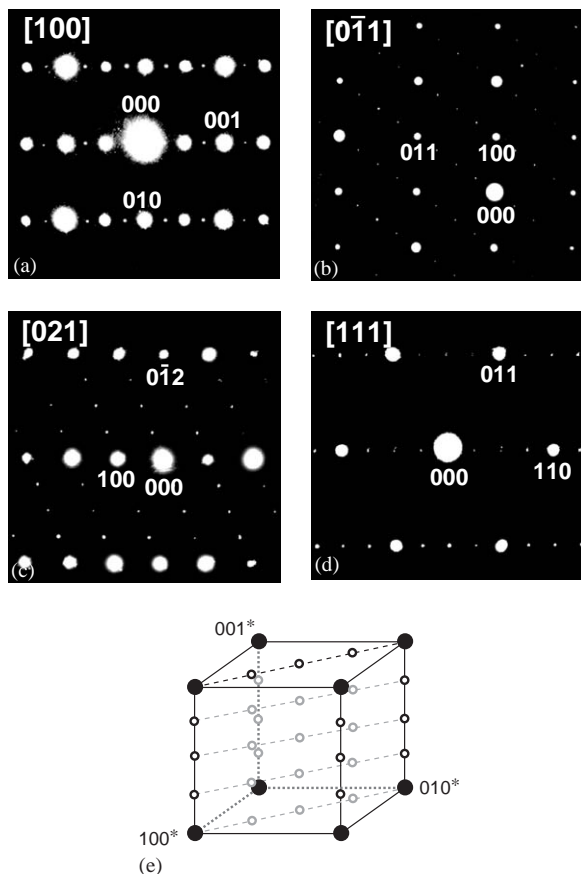


Fig. 9. The ED patterns at room temperature taken along the zone axes: (a) $[100]_p$, (b) $[011]_p$, (c) $[021]_p$ and (d) $[111]_p$. (e) the fundamental spots derived from the primitive cubic perovskite (solid circles) and the superspots derived from the CO/OO (open circles), plotted on the reciprocal lattice.

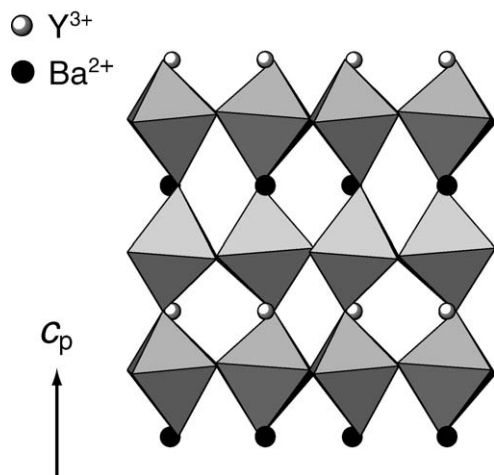


Fig. 10. A $[110]_p$ view of YBaMn_2O_6 at 350 K, where polyhedra represent MnO_6 octahedra, open circles Y^{3+} , and shaded circles Ba^{2+} , demonstrating the significant distortion of the octahedra.

layers are elongated ($\langle d_{\text{O(pl)}-\text{O(ap)}} \rangle = 2.89(3) \text{ \AA}$ for Mn(1) and $2.87(3) \text{ \AA}$ for Mn(2)). Intermediate values are obtained for the mean distances between the planar

oxygen ions ($\langle d_{\text{O(pl)}-\text{O(pl)}} \rangle = 2.80(2) \text{ \AA}$ for Mn(1) and $2.74(2) \text{ \AA}$ for Mn(2)). The Mn ions shift from the ideal position ($z = 0.25$) as well toward the YO layer. Similar structural feature, that is, the deviation from the rigid MnO_6 octahedron, has been observed for the A-site ordered $\text{LaBaMn}_2\text{O}_6$ which has the space group $P4/mmm$ [3]. However, $\text{LaBaMn}_2\text{O}_6$ has only one crystallographically equivalent site in Mn and apical and planar oxygen and each octahedron is much less distorted.

4.2. Anomalous octahedral tilting

For the purpose of dictating the octahedral tilting systems along with corresponding space groups, it is convenient to use Glazer's notation [11–13]. Fig. 11(a) shows that the MnO_6 octahedra in the PI phase are

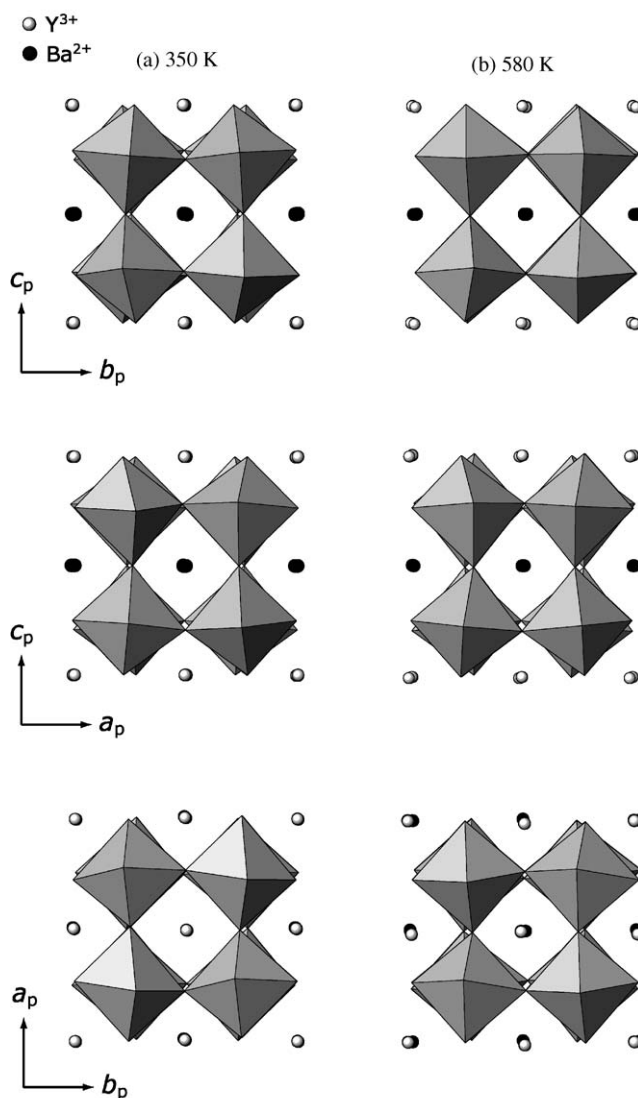


Fig. 11. The octahedral tilting of YBaMn_2O_6 projected along a_p , b_p and c_p , indicating (a) $a^-b^-c^-$ at 350 K and (b) $a^0b^-c^-$ at 580 K.

staggered when viewed along any direction, $[100]_p$, $[010]_p$, $[001]_p$. It follows that one can approximately write it as $a^-b^-c^-$, namely a three-tilt system, although the octahedron itself is heavily distorted as discussed above and the space group may not be reproduced. The octahedral tilting in the PM_2 phase is approximately described as $a^-b^-c^-$ as well. This is naturally understood because structural parameters for the PM_2 phase are almost similar to those for the PI phase, except the difference in size between the inequivalent MnO_6 octahedra. Interestingly, as shown in Fig. 11(b), the octahedra in the PM_1 phase are connected in the *trans*-configuration along the b_p - and c_p -axis, while those along the a_p -axis are connected in the *cis*-configuration. Accordingly the tilting system can be approximately regarded as $a^0b^-c^-$.

It is well known for ordinary perovskite system (ABO_3) that tilting systems vary solely with f , namely, the size mismatch between the AO and BO_2 layers. According to the experimental and theoretical considerations [12,13], non-zero tilting is realized in general when f is smaller than 1. In other words, the absence of octahedral tilting (the zero tilting system) is seen for $f > 1$. In the present system, the MnO_2 layers are sandwiched by the BaO and YO layers, resulting in a competition between two possible tilting systems responsible for $f_1 = 1.07$ and $f_2 = 0.92$, respectively. Therefore, the observed tilting systems of $YBaMn_2O_6$, $a^0b^-c^-$ for $T_{c1} < T$ and $a^-b^-c^-$ for $T < T_{c1}$, should be dominated by the role of YO layers over the BaO layers. It is interesting to note that the zero tilting ($a^0a^0c^0$) is obtained when the apical oxygen deficiency is introduced in the YO layers of $YBaMn_2O_5$ [5] or the Y^{3+} ions are replaced by the La^{3+} ions with a larger ionic radius [3]. In these two cases, the BaO layers should take the initiative in determining the tilting system.

The modification of the tilting system from $a^0b^-c^-$ to $a^-b^-c^-$ at T_{c1} clearly explains why the structural transition from the pseudo-orthorhombic (PM_1) to the pseudo-tetragonal system (PM_2) is observed. The pseudo-orthorhombicity ($a_p \neq b_p \neq c_p$) above T_{c1} is explained in terms of the tilting anisotropy along the a_p axis together with the anisotropy caused by the metal ordering along the c -axis. The pseudo-tetragonal symmetry ($a_p \cong b_p \neq c_p$) below T_{c1} can be naturally explained by the *trans*-configurations along all primitive axes. The temperature-induced transformation of octahedral tilting systems has been often observed for perovskites and layered perovskites as in $CaTiO_3$ [14] and $CaGeO_3$ [15], and discussed in connection with the theoretical possible sequence of space group (groups–subgroup relationship) as demonstrated by Aleksandrov [16] and Howard and Stokes [17]. It is commonly found that the tilting transformation is such that the number of tilt increases upon cooling. This tendency is also seen in $YBaMn_2O_6$, where two-tilt to three-tilt occurs upon cooling,

although we have to admit that there is symmetry increase.

The symmetry increase upon cooling is quite rare. An example is found in $CdPS_3$, whose monoclinic $C2/m$ space group at room temperature changes into a rhombohedral $R3$ space group below 228 K, accompanied by the change in the stacking mode [18]. They argue that this transition occurs due to a complex interplay between the layers, taking into account van der Waals forces, short-range repulsions and HOMO/LUMO interactions. In the present compound, such unusual transition with tilting change would come from the internal strain induced by the A -site ordering and from the kinetic energy of the e_g electrons stabilized by the $d_{x^2-y^2}$ ordering (see Section 4.3).

4.3. Charge and orbital ordering

As addressed in Section 3.5, the PI phase has superreflections with the q modulation. In addition, the four-fold periodicity has been observed along the c direction. Since the q modulation has been frequently obtained for $A_{1-x}A'_xMnO_3$ with x being close to 0.5 [19,20], it is straightforward to ascribe it to the CO and OO of the CE type. However, the observed quadruplication along the c -axis is incompatible with the original CE structure, in which the CE -type layers uniformly stack along the c -axis. We thus propose a new superstructure, a *modified CE* ordering pattern, where the CE -type layers stack with the sequence $[\alpha\alpha\beta\beta\dots]$ as illustrated in Fig. 12(a). The elaboration of this superstructure and the reformation of the CO/OO pattern induced by the spin-ordering below T_{c3} have been given in Ref. [7]. It is interesting to address that other groups have claimed similar CO/OO structures in $TbBaMn_2O_6$ [21,22] and $SmBaMn_2O_6$ [22]. The proposed ordering patterns are different from each other as to how the CE -type layers are built up, presumably due to the difference in ionic radius between Y and Tb (Sm), and/or to slight difference in synthetic conditions. The systematic understanding of the CO/OO patterns as well as controlling the synthetic conditions is needed.

One of the most characteristic features in $YBaMn_2O_6$ is the presence of the PM_2 phase. In the ordinary solid solution of $A_{0.5}A'_{0.5}MnO_3$, the MI transition to the CO/OO state with the CE structure is always accompanied by the drastic first-order structural phase transition [1]. In $YBaMn_2O_6$, however, the metallic behavior is retained in the PM_2 phase despite the drastic first-order structural phase transition at T_{c1} , where the magnetic interactions abruptly change as derived from the $\chi - T$ curve. Add to this, the unusual structural transition at T_{c1} from the low- T pseudo-tetragonal (monoclinic) to the high- T pseudo-orthorhombic (triclinic), suggest that a hidden parameter may play a role in compensating for the lattice entropy. We propose here the ab -plane OO in

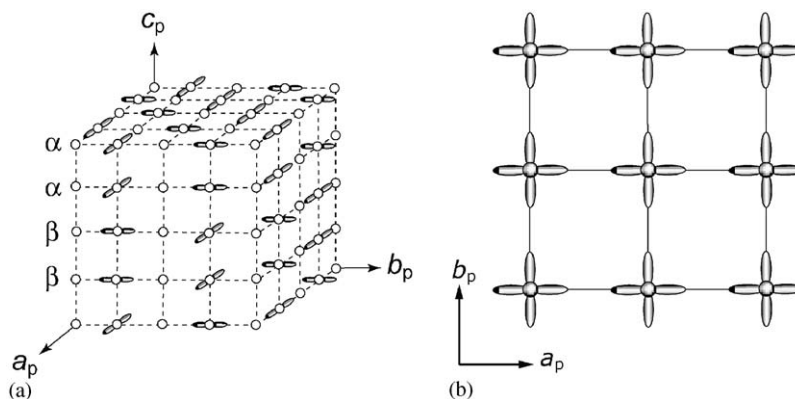


Fig. 12. (a) Modified CE-type charge/oo pattern with a four-fold periodicity ($\alpha\alpha\beta\beta$) along the c -axis for the PI state. The lobes indicate the $d_{3x^2-r^2}/d_{3y^2-r^2}$ type orbital at the Mn^{3+} sites, while the circles denote the Mn^{4+} sites. (b) Proposed $d_{x^2-y^2}$ type oo pattern for the PM_2 state.

the PM_2 phase, in which not the $d_{3x^2-r^2}/d_{3y^2-r^2}$ orbitals (responsible for the insulating CE structure below T_{c2}) but the $d_{x^2-y^2}$ orbitals are occupied as illustrated in Fig. 12(b). The increase of $(a_p + b_p)/2$ at T_{c1} and the decrease of c_p (see Fig. 3) is favorable to this oo state, and the peculiar lattice distortion in the PM_1 phase arising both from the layered structure and octahedral tilting may be relaxed by the oo. The formation of the two-dimensional $d_{x^2-y^2}$ band in the PM_2 phase would be ascribed to kinetic energy gain of the e_g electrons and predict a significant anisotropy between in-plane and out-of-plane electric resistivity, although single crystals have not been available yet.

The $d_{x^2-y^2}$ oo (accompanied by the A-type spin ordering) has been reported for $A_{1-x}A'_x\text{MnO}_3$, where x is close to 0.5 and f is slightly smaller than 1. $\text{Nd}_{1-x}\text{Sr}_x\text{MnO}_3$ is a typical example [23,24]. It should be pointed out that in the metal-disordered systems this state tends to coexist with the insulating $d_{3x^2-r^2}/d_{3y^2-r^2}$ oo state of the CE type. The coexistence of the two states has been experimentally detected by the neutron diffraction experiment, and the volume fraction of each state is reported to change with T . On the contrary, our neutron diffraction study indicates no sign of the electronic phase separation. Instead, each phase appears independently as a function of T . It is possible that, because of the absence of the lattice disorder and inhomogeneity in YBaMn_2O_6 , the electronic phase separation, typically observed in the metal-disordered systems, is completely suppressed but replaced by the distinct and successive transitions.

4.4. Extremely high MI transition temperature

Finally, we would like to discuss why the MI transition temperature ($T_{\text{MI}} = T_{c2} = 480 \text{ K}$) in YBaMn_2O_6 is extremely high, in comparison with half-doped metal-disordered system $A_{0.5}A'_{0.5}\text{MnO}_3$. It is known that f is structurally correlated with the oxygen

bridging angle $\angle \text{Mn-O-Mn}$, and the deviation of $\angle \text{Mn-O-Mn}$ from 180° destabilizes the FM state. According to the phase diagram plotted against f for $A_{0.5}A'_{0.5}\text{MnO}_3$, the CO/oo state of the CE type appears for $f < 0.975$ [1] and T_{MI} increases with decreasing f . However, this view can not be directly applied to YBaMn_2O_6 , since the structure has the averaged angles of $\langle \angle \text{Mn-O(pl)-Mn} \rangle = 165.7(8)^\circ$ and $\langle \angle \text{Mn-O(ap)-Mn} \rangle = 167.9(7)^\circ$ (in the PI state), which are much larger than $\angle \text{Mn-O(pl)-Mn} = 161.8(1)^\circ$ and $\angle \text{Mn-O(ap)-Mn} = 158.0(3)^\circ$ in $\text{La}_{0.5}\text{Ca}_{0.5}\text{MnO}_3$ having much smaller $T_{\text{MI}} \sim 170 \text{ K}$ [25].

The first possible reason for the extremely high T_{MI} is the absence of the randomness in the lattice owing to the Y/Ba ordering. It is probable in metal-disordered system that the structural randomness suppresses the correlation length for the CO/oo state and descends T_{MI} . Second, the heavily distorted and tilted MnO_6 octahedra should play a key role. In the case of disordered manganese perovskite, one usually obtains only one crystallographically site for Mn, O(pl) and O(ap), giving rise to unique $\angle \text{Mn-O(pl)-Mn}$ and $\angle \text{Mn-O(ap)-Mn}$. This is not the case for YBaMn_2O_6 , where the $\angle \text{Mn-O-Mn}$ angles take various values, ranging from $157.5(8)^\circ$ to $176.8(8)^\circ$ in the PI state (see Table 2). The destabilization of the FM state may be understood in terms of the percolation model, taking some *metallic* Mn–Mn bonds (with higher angles) and other *insulating* Mn–Mn bonds (with lower angles) into consideration. In other words, the large distribution of angles results in narrowing the *effective* band width w in YBaMn_2O_6 , thus destabilizing the FM state and alternatively stabilizing the CO/oo state.

5. Summary

Relation between structures and physical properties of the metal-ordered manganite perovskite YBaMn_2O_6

was investigated. A high-temperature metallic phase ($T_{c1} < T$) was solved in the triclinic space group $P1$. The MnO_6 octahedra are tilted like $a^0b^-c^-$. At the first order transition T_{c1} , the structure becomes the monoclinic $P2$ with the octahedral tilting system of $a^-b^-c^-$. The $d_{x^2-y^2}$ OO is proposed for the PM_2 phase. While the monoclinic space group $P2$ is retained across T_{c2} , two crystallographically inequivalent MnO_6 octahedra show a distinct volume difference. This is in agreement with the resistivity measurement that shows the MI transition, accompanied by the CO with the checkerboard pattern in the ab plane. TEM further revealed the *modified CE* type of the CO/OO. The extremely high MI transition temperature can be accounted by the absence of the randomness in the lattice and the heavily distorted and tilted octahedra.

Acknowledgments

This work is partly supported by Grants-in-Aid for Scientific Research Nos. 40302640, 407 and 758 and for Creative Scientific Research (No. 13NP0201) from the Ministry of Education, Culture, Sports, Science and Technology, Japan. The authors thank Prof. A.N. Vasil'ev, Dr. J. Yamaura, Dr. C. Michioka and Dr. Matsushita for valuable discussions.

References

- [1] C.N.R. Rao, B. Raveau (Ed.), *Colossal Magnetoresistance, Charge Ordering and Related Properties of Manganese Oxides*, World Scientific, Singapore, 1998.
- [2] B.M. Letfulov, J.K. Freericks, *Phys. Rev. B* 64 (2001) 174409.
- [3] F. Millange, V. Caignaert, B. Domengés, B. Raveau, E. Suard, *Chem. Mater.* 10 (1999) 1974.
- [4] T. Nakajima, H. Kageyama, Y. Ueda, *J. Phys. Chem. Solids* 63 (2002) 913.
- [5] T. Nakajima, H. Kageyama, H. Yoshizawa, Y. Ueda, *J. Phys. Soc. Jpn.* 71 (2002) 2843.
- [6] F. Millange, E. Suard, V. Caignaert, B. Raveau, *Mater. Res. Bull.* 34 (1999) 1.
- [7] H. Kageyama, T. Nakajima, M. Ichihara, Y. Ueda, H. Yoshizawa, K. Ohoyama, *J. Phys. Soc. Jpn.* 72 (2003) 241.
- [8] F. Izumi, T. Ikeda, *Mater. Sci. Forum* 321–324 (2000) 198.
- [9] I.D. Brown, D. Altermatt, *Acta Crystallogr. B* 41 (1985) 244.
- [10] R.D. Shannon, C.T. Prewitt, *Acta Crystallogr. B* 25 (1969) 925.
- [11] A.M. Glazer, *Acta Crystallogr. B* 28 (1972) 3384.
- [12] P.M. Woodward, *Acta Crystallogr. B* 53 (1997) 32.
- [13] P.M. Woodward, *Acta Crystallogr. B* 53 (1997) 44.
- [14] B.J. Kennedy, C.J. Howard, B.C. Chakoumakos, *J. Phys.: Condens. Matter* 11 (1999) 1479.
- [15] X. Liu, Y. Wang, R.C. Liebermann, P.D. Maniar, A. Norvotsky, *Phys. Chem. Minerals* 18 (1991) 224.
- [16] K.S. Aleksandrov, *Ferroelectrics* 14 (1976) 801.
- [17] C.J. Howard, H.T. Stokes, *Acta Crystallogr. B* 54 (1998) 782.
- [18] F. Boucher, M. Evain, R. Brec, *Acta Crystallogr. B* 51 (1995) 952.
- [19] Y.Q. Wang, X.F. Duan, Z.H. Wang, B.G. Shen, *Mater. Sci. Eng. A* 333 (2002) 80.
- [20] N. Fukumoto, S. Mori, N. Yamamoto, Y. Moritomo, T. Katsufuji, C.H. Chen, S-W. Cheong, *Phys. Rev. B* 60 (1999) 12963.
- [21] A.J. Williams, J.P. Attfield, *Phys. Rev. B* 66 (2002) 220405.
- [22] T. Arima, D. Akahoshi, K. Oikawa, T. Kamiyama, M. Uchida, Y. Matsui, Y. Tokura, *Phys. Rev. B* 66 (2002) 140408.
- [23] R. Kajimoto, H. Yoshizawa, H. Kawano, Y. Tokura, K. Ohoyama, M. Ohashi, *Phys. Rev. B* 60 (1999) 9506.
- [24] Y. Moritomo, T. Akimoto, A. Nakamura, K. Ohoyama, M. Ohashi, *Phys. Rev. B* 58 (1998) 5544.
- [25] P.M. Woodward, T. Vogt, D.E. Cox, A. Arulraj, C.N.R. Rao, P. Karen, A.K. Cheetham, *Chem. Mater.* 10 (1998) 3652.